This article has been accepted for publication in a future issue of this journal, but has not been fully edited. Content may change prior to final publication. Citation information: DOI 10.1109/TIE.2020.3034867, IEEE Transactions on Industrial Electronics

Low Frequency Medium Power Capacitor-Free Self-Resonant Wireless Power Transfer

Chaoqiang Jiang, *Member, IEEE*, Daniel E. Gaona, *Student Member, IEEE*, Yanfeng Shen, *Member, IEEE*, Hui Zhao, *Member, IEEE*, K. T. Chau, *Fellow, IEEE*, and Teng Long, *Member, IEEE*

***Abstract*- With the rapid development of wireless power transfer (WPT), the self-resonant WPT system without using additional compensation capacitors has attracted attention. However, most of reported self-resonant WPT systems have low power transfer (less than 100 W) and high operating frequencies at megahertz. In this paper, four multi-layer, self-resonant WPT coil pads with different dielectrics are designed and experimentally validated. The aim of this paper is to increase the power rating and decrease the operating frequency for capacitor-free WPT system compared to reported systems used in consumer electronics. Analysis of integrated compensation capacitance, inductance, and parasitic capacitance of the coil is provided. Finite Element Analysis (FEA) is used to evaluate four dielectric materials, mica, polypropylene, polyimide, and fiberglass. An experimental setup has been developed, which can achieve more than 360 W power transfer for a 120 mm air gap with an efficiency of 82% and an operating frequency of near 80 kHz.**

***Index Terms*- Wireless power transfer, capacitor-free, self-resonant, dielectrics.**

I. Introduction

WIRELESS power transfer (WPT) concept using two-loop resonators has been reported for more than one hundred years by Nikola Tesla [1-3]. As so far, by the advantages of cableless and electrical isolation, the WPT technology has been used in many applications such as charging, heating, and lighting [4, 5]. Most importantly, the WPT technique is getting more and more attention due to the rapid development of portable electronics, implanted medical devices, and electric vehicles (EVs) [6, 7].

The WPT utilizes the electromagnetic field to constitute the power flow path. In order to generate and receive the coupling magnetic fluxes, the transmitter and receiver coil pads are needed but the coupling coefficient is low due to the large air gap. A resonant circuit is required to reduce the voltage-to-current rating. As a result, high frequency and high voltage compensation capacitors are required, which increases the complexity and cost and reduces reliability. Thus, a self-resonant coil where the compensation capacitor is integrated within the pad is desirable. System compactness is attractive to medium power applications, such as the autonomous mobile robot (AMR), electric unicycle or scooter, and unmanned aerial vehicle (UAV) [8-10], where space and weight constraints on specific dimensions such as the height and weight are more demanding.

Particular coil parasitic capacitance from the coil structure can be utilized to replace the compensation capacitor. In order to achieve the integrated capacitance between coil turns, the bifilar coil topology is popular to constitute the self-resonant circuit. There are two main types: open-end coil and short-end coil [11]. The open-end coil is equivalent to an inductor with a series connected capacitor, which has been commonly used as the compensation network [12]. The short-end coil is equivalent to an inductor with a parallel connected capacitor. By using the open-end coil topology, a multi-frequency self-resonant WPT system has been presented with the resonant frequencies of 2.5 MHz and 13 MHz [13]. Besides, the parasitic capacitance of saline water filled helical coil was used to transfer the wireless power underwater [14].

Printed rectangular and spiral coils have been used for self-resonant WPTs. A short-end coil with double layer printed spiral coil topology, which is able to transmit power of 150 W at the frequency of 4 MHz, was presented in [15]. To increase efficiency, high quality factor self-resonant structures were investigated for mobile device charging [16]. However, current researches are limited to frequencies in the order of hundreds of kilohertz and megahertz [17-19]. The capacitor-free self-resonant WPT topology with lower frequency and medium power rating (hundreds of Watts) is absent.

In this paper, four-layer capacitor-free, self-resonant WPT coil structures with different dielectrics are designed and experimentally validated. The key is to integrate the capacitor and inductor into a single coil pad. Common dielectric materials mica, polypropylene, polyimide, and fiberglass sheets are adopted to compare the proposed structure. The low frequency (less than 100 kHz) medium power (more than 300 W) capacitor-free multi-layer coil can be potentially applied on some curved surfaces of the appliances due to the coil flexibility and thickness [20, 21].

In Section II, the typical WPT system is presented. In Section III, modeling of the proposed capacitor-free WPT coil including inductance and capacitance calculation is discussed. In Section IV, simulation and measurement of four self-resonant coils are compared. In Section V, an experimental prototype is tested to verify the feasibility of the proposed topology. A conclusion is drawn in Section VI.

Manuscript received Month xx, 2020; revised Month xx, 2020; accepted Month xx, 2020. (*Corresponding author: Teng Long*).

C. Jiang, D. E. Gaona, Y. Shen, H. Zhao, and T. Long are with the Department of Engineering–Electrical Engineering Division, University of Cambridge, Cambridge CB3 0FA, U.K. (e-mail: cj426@cam.ac.uk, deg32@cam.ac.uk, ys523@cam.ac.uk, hz352@cam.ac.uk, tl322@cam.ac.uk).

K. T. Chau is with the Department of Electrical and Electronic Engineering, The University of Hong Kong, Hong Kong. (email: ktchau@eee.hku.hk).

This article has been accepted for publication in a future issue of this journal, but has not been fully edited. Content may change prior to final publication. Citation information: DOI 10.1109/TIE.2020.3034867, IEEE Transactions on Industrial Electronics

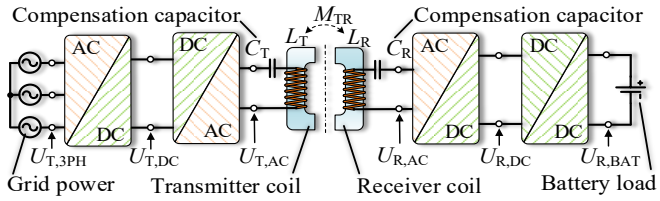

Fig. 1. Typical topology of the WPT system with series-series compensation for wireless battery charging.

II. Typical WPT System

As depicted in Fig. 1, the transmitter side consists of an AC-DC converter connected to the main grid, a high frequency DC-AC inverter, and a transmitter coil and compensation circuitry (the series capacitor compensation in this case). The receiver side normally consists of the identical or similar coil and compensation circuitry and an additional DC-DC converter for battery charging. As shown in Fig. 1, L_T and L_R are the inductance of the transmitter coil and the receiver coil; M_{TR} is the mutual inductance between the transmitter coil and the receiver coil; C_T and C_R are the compensation capacitors of the transmitter side and the receiver side; $U_{T,DC}$ and $U_{T,AC}$ are the output RMS voltages of the AC-DC converter and DC-AC converter at the transmitter side; $U_{R,AC}$ and $U_{R,DC}$ are the input RMS voltages of the AC-DC converter and DC-DC converter at the receiver side; $I_{T,AC}$ and $I_{R,AC}$ are the RMS currents of the transmitter coil and the receiver coil.

When the operating frequency is set at ω, the WPT system can be described in voltage equations as

$$\begin{cases} I_{T,AC}(R_{Tcoil}+1/(j\omega C_T)+j\omega L_T)+j\omega M_{TR}I_{R,AC}=U_{T,AC} \\ j\omega M_{TR}I_{T,AC}+I_{R,AC}(R_{Rcoil}+1/(j\omega C_R)+j\omega L_R+R_{Lac})=0 \end{cases} \quad (1)$$

where R_{Tcoil}, R_{Rcoil} and R_{Lac} are the resistances of the transmitter coil, the receiver coil, and the equivalent load of the receiver side AC-DC rectifier. The equivalent series resistance (ESR) of the compensation capacitors is neglected.

Thus, the input power $P_{IN,AC}$ of transmitter LC tank and the output power $P_{OUT,AC}$ of receiver LC tank are

$$\begin{cases} P_{IN,AC}=U_{T,AC}I_{T,AC}=\left|\dfrac{{U_{T,AC}}^2 Z_{R,AC}}{(M_{TR}\omega)^2+Z_{T,AC}Z_{R,AC}}\right| \\ P_{OUT,AC}={I_{R,AC}}^2 R_{Lac}=\left|\dfrac{{M_{TR}}^2\omega^2{U_{T,AC}}^2 R_{Lac}}{((M_{TR}\omega)^2+Z_{T,AC}Z_{R,AC})^2}\right| \end{cases} \quad (2)$$

where $Z_{R,AC}$ and $Z_{T,AC}$ can be expressed as

$$\begin{cases} Z_{R,AC}=R_{Rcoil}+1/(j\omega C_R)+j\omega L_R+R_{Lac} \\ Z_{T,AC}=R_{Tcoil}+1/(j\omega C_T)+j\omega L_T \end{cases} \quad (3)$$

Then, the coil-to-coil transmission efficiency $\eta_{AC\text{-}AC}$ is

$$\eta_{AC-AC}=\frac{P_{OUT,AC}}{P_{IN,AC}}=\left|\frac{{M_{TR}}^2\omega^2 R_{Lac}}{((M_{TR}\omega)^2+Z_{T,AC}Z_{R,AC})Z_{R,AC}}\right|\times 100\% \quad (4)$$

In order to achieve the maximum power transmission efficiency, the operating frequency should equal the resonant frequency ω_o of both the transmitter and the receiver LC tanks:

$$\omega=\omega_0=1/\sqrt{L_T C_T}=1/\sqrt{L_R C_R} \quad (5)$$

With the identical transmitter coil and receiver coil, the maximum transmission efficiency can be achieved when the currents in both coils are the same, where the AC equivalent load R_{Lac} equals $\omega_o M_{TR}$. For the experiment, the DC load R_{Ldc} after the AC-DC converter at the receiver side is set as

$$R_{Ldc}=\pi^2\omega_o M_{TR}/8 \quad (6)$$

In the resonant circuit, high voltage will be produced due to the high frequency and high current. As a result, several series and parallel connected capacitors have to be employed to withstand the high voltage, which increases the cost and complexity and reduces the reliability of the system.

III. Modeling of Proposed Capacitor-free WPT

The proposed capacitor-free self-resonant WPT coil pad is shown in Fig. 2(a), consisting of four main parts: the copper foils, the dielectric, the adhesions for foil and dielectric, and the ferrite core. The proposed capacitor-free coil pad is designed with outer size of 270mm × 270 mm and inner size of 180mm × 180 mm. The thickness of the pad depends on the number of layers for the coil windings.

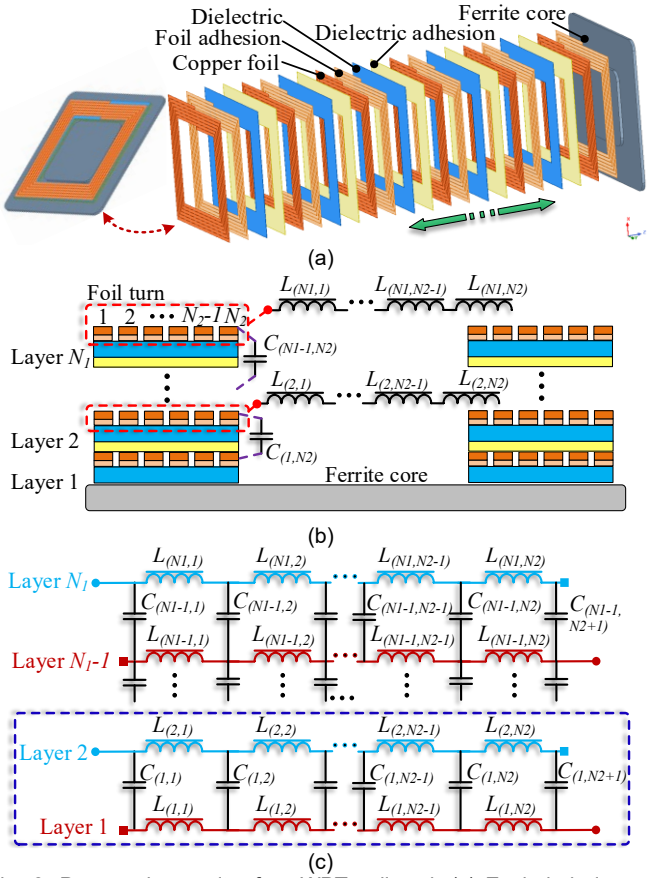

Fig. 2. Proposed capacitor-free WPT coil pad. (a) Exploded view of multi-layer coil structure. (b) Sectional view of integrated capacitors and inductors. (c) Equivalent circuit of multi-layer coils.

A. Equivalent Circuit Model of Two-layer Coil

As shown in Fig. 2(b), the copper foil stenciled in spiral traces for coils, foil adhesion, dielectric sheet and dielectric adhesion are stacked to form one coil layer. Multiple layers are assembled together to form the self-resonant winding for the pad. In each copper foil, any turn out of the total N_2 turns of the coil can be regarded as a one-turn inductor as denoted by $L_{(N1,N2)}$. As shown in Fig. 2(c), the capacitance between each turn and the adjacent layer can be lumped into a capacitor as denoted by $C_{(N1-1,N2)}$ for analysis simplification. The coil layers are alternatively series connected, i.e., Layer 1 series connected

This article has been accepted for publication in a future issue of this journal, but has not been fully edited. Content may change prior to final publication. Citation information: DOI 10.1109/TIE.2020.3034867, IEEE Transactions on Industrial Electronics

to Layer 3, Layer 5 and Layer *2n-1*; Layer 2 series connected to Layer 4, Layer 6 and Layer *2n*.

Inductance and lumped capacitors are considered identical due to the symmetrical layout and materials of coils. Therefore:

$$\begin{cases} C_{(1,n)} = C_{(2,n)} = \cdots = C_{(N1-1,n)}, n = 1,2,\cdots,N_2+1 \\ L_{(1,n)} = L_{(2,n)} = \cdots = L_{(N1,n)}, n = 1,2,\cdots,N_2 \end{cases} \tag{7}$$

The voltage equations in two-layer coil system are [22]

$$\begin{cases} V_{L_{(1,1)}} = V_{L_{(2,1)}}, V_{L_{(1,2)}} = V_{L_{(2,2)}}, \cdots, V_{L_{(1,n)}} = V_{L_{(2,n)}} \\ V_{C_{(1,1)}} + \sum_{i=1}^{n} V_{L_{(2,i)}} = V_{C_{(1,n+1)}} + \sum_{i=1}^{n} V_{L_{(1,i)}} \quad (n = 1,2,\cdots,N_2) \end{cases} \tag{8}$$

where $V_{L(1,n)}$ and $V_{L(2,n)}$ are the voltages across the n_{th} inductor at Layer 1 and Layer 2, respectively. $V_{C(1,n)}$ is the voltage across the n_{th} capacitor between the two layers.

From (8), voltages across all distributed capacitors $C_{(1,n)}$ between Layer 1 and Layer 2 are identical although their capacitances are different. The two-layer coil pad consists of multiple loops and each loop has an equivalent circuit of two pairs of capacitors and inductors, i.e. $C_{(1,N2)}$ and $L_{(2,\ N2)}$ as one pair and the $C_{(1,\ N2+1)}$, $L_{(2,\ N2+1)}$ as the other as shown in Fig. 3(a). Due to the symmetrical layout and coil materials, the inductances of every n_{th} turn at different layers are identical, so are the voltages $V_{L(1,N2)}$ and $V_{L(2,N2)}$ across the inductors. Thus, the voltages $V_{C(1,N2)}$ and $V_{C(1,N2+1)}$ across capacitor N_2 and N_{2+1} are identical. The same deduction can be adopted to the next loop until all single loops are completed. Then the capacitor voltage can be expressed as

$$\begin{cases} V_{C_{(1,1)}} = V_{C_{(1,n)}} \\ V_{C_{(i,1)}} = V_{C_{(i,n)}} \end{cases} (n = 1,2,\cdots,N_2+1; i = 1,2,...,N_1) \tag{9}$$

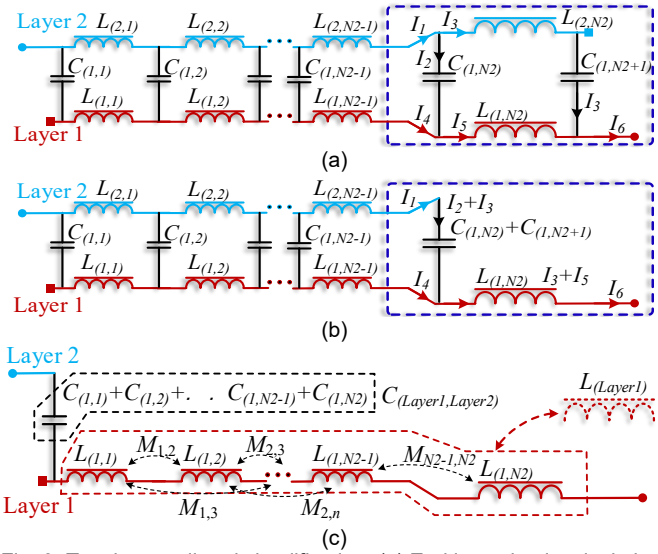

Fig. 3. Two-layer coil pad simplification. (a) End loop circuit calculation. (b) End loop equivalent circuit after simplification. (c) Two-layer coil equivalent circuit.

As shown in the dashed area of Fig. 3(a), I_1 and I_4 are the input currents into the end loop circuit, I_6 is the output current from the end loop. Then, I_1 can be expressed as

$$\begin{aligned} I_1 &= C_{(1,N2)} \frac{dV_{C_{(1,N2)}}}{dt} + C_{(1,N2+1)} \frac{dV_{C_{(1,N2+1)}}}{dt} \\ &= (C_{(1,N2)} + C_{(1,N2+1)}) \frac{dV_{C_{(1,N2)}}}{dt} = (C_{(1,N2)} + C_{(1,N2+1)}) \frac{dV_{C_{(1,N2-1)}}}{dt} \end{aligned} \tag{10}$$

The mutual inductance between $L_{(1,\ N2)}$ and $L_{(2,\ N2)}$ can be calculated as

$$M_{(1,2,N2)} = k_{(1,2,N2)} \sqrt{L_{(1,N2)} L_{(2,N2)}} \tag{11}$$

Since the same magnetic flux linking $L_{(1,\ N2)}$ and $L_{(2,\ N2)}$ due to the same geometry, the coupling coefficient $k_{(1,\ 2,\ N2)}$ can be regarded as 1. The voltage crosses the $L_{(1,\ N2)}$ is the sum of induced voltage from and $L_{(1,\ N2)}$ and $L_{(2,\ N2)}$, which can be calculated as

$$\begin{aligned} V_{L_{(1,N2)}} &= L_{(1,N2)} \frac{dI_5}{dt} + L_{(2,N2)} \frac{dI_3}{dt} \\ &= L_{(1,N2)} \frac{d(I_3 + I_5)}{dt} = L_{(1,N2)} \frac{dI_6}{dt} \end{aligned} \tag{12}$$

Based on equations (10) and (12), the end loop circuit can be modelled as a capacitor and an inductor, as shown in Fig. 3(b). By iterating the above analysis, the entire two-layer coil can be modelled as a capacitor and an inductor as shown in Fig. 3(c). The equivalent capacitance is the sum of capacitance between Layer 1 and Layer 2, which can be calculated as a parallel-plate capacitor of the total foil area covered by different dielectrics. The calculation of the equivalent inductance will be discussed in *Section E*.

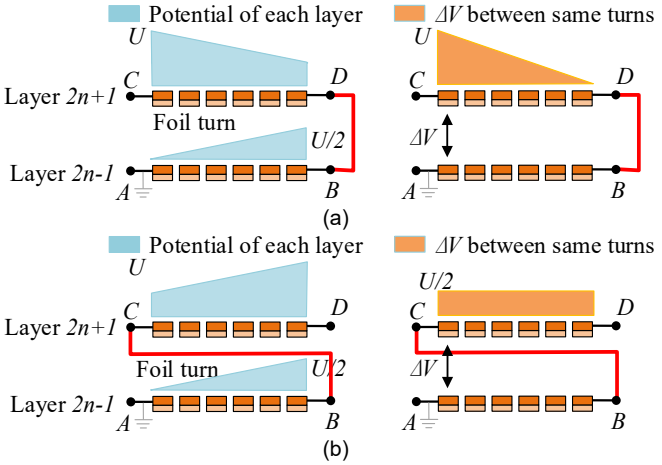

Fig. 4. Potential and voltage distributions of different layer connections. (a) Opposite direction with the sequence of A-B-D-C. (b) Same direction with the sequence of A-B-C-D.

B. Connection of Layers

As analyzed in *Section A*, the odd layer coils are series connected such as Layer *2n-3* connected to Layer *2n-1* to form an inductor as well as the even layer coils. There are two connections between two odd or even layers: opposite direction as shown in Fig. 4(a) and same direction as shown in Fig. 4(b). For both connections, the potential distribution linearly increases with respect to reference point A. However, the voltage ΔV distributions between the n_{th} of Layer *2n-1* and the n_{th} of Layer *2n+1* are not the same [23]. As shown in Fig. 4(a), the opposite direction has an unevenly distributed voltage ΔV while the same direction has an evenly one as shown in Fig. 4(b). The connection with the same direction has less

This article has been accepted for publication in a future issue of this journal, but has not been fully edited. Content may change prior to final publication. Citation information: DOI 10.1109/TIE.2020.3034867, IEEE Transactions on Industrial Electronics

electrostatic energy stored due to the even distribution of voltage, which benefits inductor design in terms of lower electric field and parasitic capacitance. Therefore, the same direction connection with the sequence of A-B-C-D is preferable and is adopted in this paper.

C. Capacitance Calculation of Adjacent Coil Layers

As shown in Fig. 5, the foil adhesion, dielectric, and dielectric adhesion are inserted within the two copper foils. The total turn-to-turn capacitance between two layers can be calculated as a planar capacitor. Thus, the total area A_{Total} of the planar plate is equal to the sum of the area of each turn.

$$A_{Total} = A_1 + A_2 + A_3 + \cdots + A_{N2} \tag{13}$$

For the proposed capacitor-free coil pad, there are three materials, foil adhesion, dielectric, and dielectric adhesion sandwiched between the two copper foils. The total capacitance between two copper foils can be regarded as three capacitors with different dielectric materials connected in series [24]. Then, the layer-to-layer capacitance $C_{Layer\text{-}to\text{-}Layer}$ is

$$C_{Layer-to-Layer} = 1/\left(\frac{d_1}{\kappa_1 \varepsilon_0 A_{Total}} + \frac{d_2}{\kappa_2 \varepsilon_0 A_{Total}} + \frac{d_3}{\kappa_3 \varepsilon_0 A_{Total}}\right) \tag{14}$$

where ε_0 is the permittivity of space, d_1, d_2, and d_3 are the thickness of the foil adhesion, dielectric and dielectric adhesion, respectively; κ_1, κ_2, and κ_3 are the relative permittivity of the foil adhesion, dielectric and dielectric adhesion, respectively.

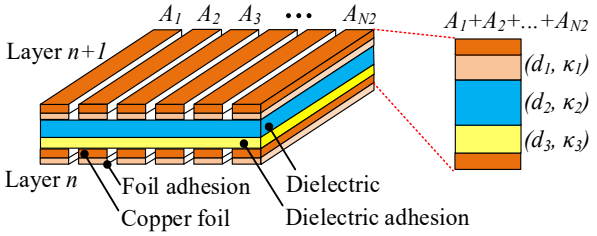

Fig. 5. Layer-to-layer capacitance calculation inserted with multiple dielectrics.

D. Single-layer Fringing Effect

Considering the parasitic electric field between turns of the single-layer coil, the parallel parasitic capacitance, which is undesirable, will be induced, especially when the distance of every two turns is small. As shown in Fig. 6, the fringing electric field is applied to four parallel connected capacitors between two conductors via the air, foil adhesion, dielectric, and the dielectric adhesion, respectively [25]. Thus, the parasitic capacitance $C_{Turn\text{-}to\text{-}Turn}$ between two turns can be expressed as

$$C_{Turn-to-Turn} = C_{air} + C_{coilad} + C_{die} + C_{diead} \tag{15}$$

where C_{air}, C_{coilad}, C_{die}, and C_{diead} are the partial capacitance with the air, the foil adhesion, dielectric, and the dielectric adhesion, respectively.

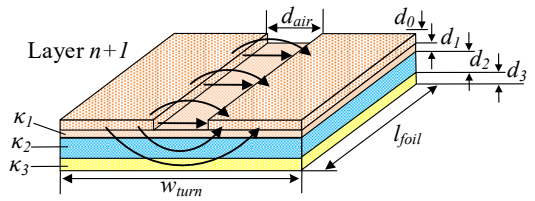

Fig. 6. Single-layer coil parasitic field distribution with multiple materials inserted.

Based on the conformal mapping and the assumption of the magnetic wall [26], each capacitance can be calculated separately. The calculation method is listed in the Appendix. For the first layer adjacent to the ferrite core, as shown in Fig. 2(b) there is no dielectric adhesion inserted. The ferrite core will have a slight variation on the fringing effect when comparing with that without ferrite core [27]. As a result, the ferrite core affects the undesirable parasitic capacitance of single coil inductor rather than the desirable series integrated compensation capacitance. The self resonant frequency is determined by the desirable compensation capacitance between coil layers while the undesirable parasitic capacitance will slightly decrease the self resonant frequency. The capacitance with the ferrite core $C_{ferrite}$ can be calculated by replacing the dielectric with the ferrite and no need to calculate the C_{diead}, as listed in the Appendix.

E. Inductance Calculation

As shown in Fig. 3(c), the single-layer coil inductance L_{Layer1} is calculated by each turn's inductance and their mutual inductances, as expressed

$$L_{Layer1} = \sum_{i=1}^{N2} L_{(1,i)} + \sum_{i}^{N2}\sum_{j}^{N2} M_{i,j} \qquad (i \neq j) \tag{16}$$

where $M_{i,j}$ is the mutual inductance between i^{th} turn and j^{th} turn at the same layer.

Since the proposed coil topology is with the square pad shape and wound by thin copper foil, the self-inductance of the single-layer coil without ferrite core can be calculated as [28]

$$L_{Layer1} = \frac{1.27\mu_0 N_2^{\,2}(l_{outer} + l_{inner})}{4}\left[\ln\left(\frac{2.07}{\varphi}\right) + 0.18\varphi + 0.13\varphi^2\right] \tag{17}$$

where μ_0 is the permeability of free space, l_{outer} and l_{inner} are the outer and inner side lengths of the square coil pad, φ is the fill factor, which is calculated by $(l_{outer} - l_{inner})/(l_{outer} + l_{inner})$.

Thus, the total inductance is calculated by

$$L_{Total} = \sum_{i=1}^{N1/2} L_{Layer(i)} + \sum_{i}^{N1/2}\sum_{j}^{N1/2} M_{Layer,i,j} \qquad (i \neq j) \tag{18}$$

where $M_{Layer,i,j}$ is the mutual inductance between i^{th} layer and j^{th} layer coil pad. The mutual inductance $M_{Layer,i,j}$ can be regarded as L_{Layer1}. Thus, the total inductance is

$$L_{Total} = \left(\frac{N_1}{2}\right)^2 L_{Layer1} \tag{19}$$

IV. Self-resonant Simulation and Coil Measurement

Four types of capacitor-free coil pads are proposed and fabricated with different dielectric materials, namely, mica, polypropylene, polyimide, and fiberglass, as shown in Fig. 7. A double-sided non-woven tape with acrylic adhesive is used between the copper foil and dielectric. The dielectric constant of acrylic adhesive is 3.6. The thicknesses of the foil adhesion and dielectric adhesion are 0.026 mm and 0.1 mm, respectively. The copper foil with a width of 6.4 mm is used to wind the coil pad. There are 6 copper foil layers, where each copper foil layer has 6 turns. The distance between two turns is set at 1.3 mm. Specifications are listed in Table I. Results of analytical calculation, finite element analysis (FEA), and measurement are compared. The FEA results are obtained with ANSYS Maxwell and the measured results are from the N4L Phase Sensitive Multimeter PSM3750.

This article has been accepted for publication in a future issue of this journal, but has not been fully edited. Content may change prior to final publication. Citation information: DOI 10.1109/TIE.2020.3034867, IEEE Transactions on Industrial Electronics

TABLE I. Specifications of Different Capacitor-free Coil Pads

Items	Mica	Polypropylene	Polyimide	Fiberglass
Thickness (mm)	0.2	0.127	0.152	0.229
Dielectric constant	2.8	2.3	4.0	5.5
Dielectric strength (kV/mm)	25	57.5	39.5	19.7

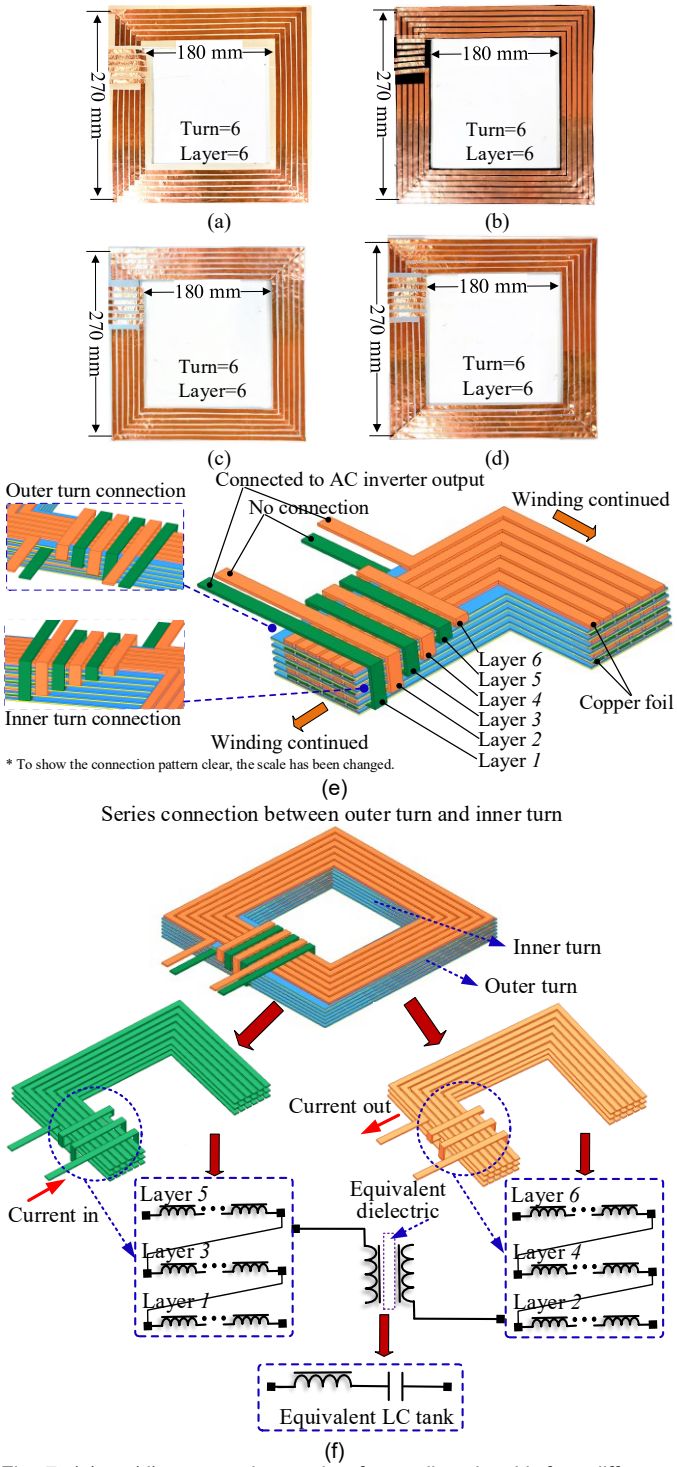

Fig. 7. (a) to (d) proposed capacitor-free coil pads with four different dielectric materials. (e) 3D view of six-layer structure and connection. (f) Connection of Group 1 (turns on the Layer 1, Layer 3, Layer 5) and Group 2 (turns on the Layer 2, Layer 4, and Layer 6), each Group has one terminal open-circuited and the other connected to the AC output of the rectifier/inverter. Two Groups are connected via integrated capacitor as designed to form a series compensation circuit as a LC tank.

As shown in Fig. 7(e), turns on six layers are divided into two single inductors, where turns on Layer 1, 3, and 5 are directly series connected as Group 1 and so do the turns of Layer 2, 4, and 6 as Group 2. For one single inductor, the connection pattern is shown in Fig. 7(f), where the inner turn of Layer 2 is series connected to the outer turn of Layer 4 as an example. One terminal of each Group is connected to the AC output of the rectifier/inverter and the other is open-circuited. Only the inner turn of Layer 1 and the outer turn of Layer 6 are directly connected to the AC rectifier/inverter output, while the inner turn of Layer 2 and the outer turn of Layer 5 are open-circuited. By using this structure, turns of each Group are directly connected by conductors but turns between Groups are connected via the integrated capacitor as designed. Therefore, the integrated capacitor is equivalently connected in series with the inductor to form the compensation circuit, as shown in Fig. 7(f).

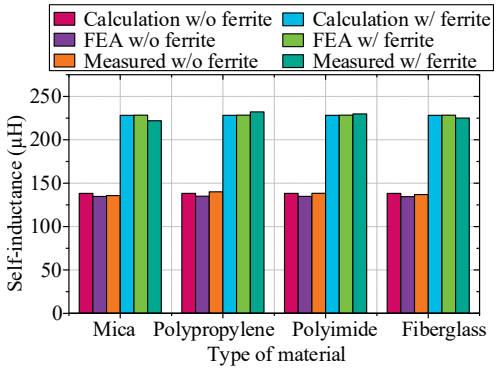

Fig. 8. Self-inductance results from theoretical calculation, FEA simulation, and experimental measurement at 85 kHz.

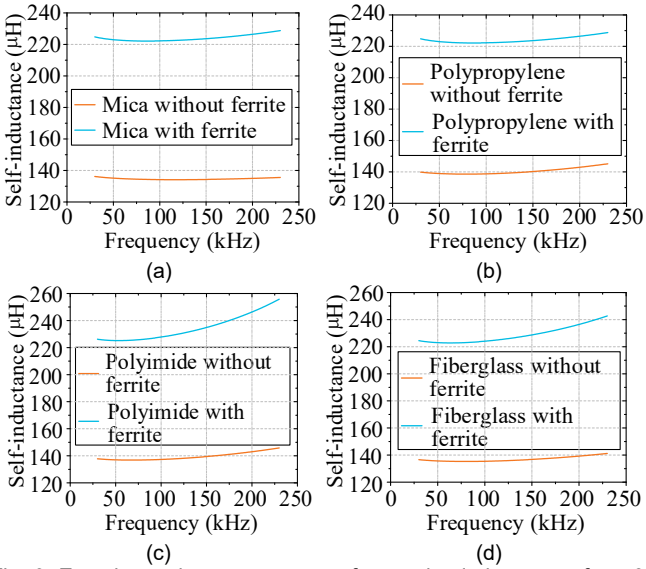

Fig. 9. Experimental measurements of sweeping inductances from 30 kHz to 230 kHz. (a) With mica dielectric. (b) With polypropylene dielectric. (c) With polyimide dielectric. (d) With fiberglass dielectric.

A. Self-inductance

As shown in Fig. 8, the self-inductance results among theoretical calculation, FEA simulation, and experimental measurement at 85 kHz are compared between pads with and without ferrite cores. It can be found that the inductance of different materials has a negligible difference. As shown in Fig.

This article has been accepted for publication in a future issue of this journal, but has not been fully edited. Content may change prior to final publication. Citation information: DOI 10.1109/TIE.2020.3034867, IEEE Transactions on Industrial Electronics

9, the self-inductances are measured from 30 kHz to 230 kHz. The inductance at the frequency range of 80~90 kHz shows small variations. In addition, the inductance with ferrite core shows slight variations within 1.9% on horizontal misalignments, while large variations under very low airgaps, as shown in Fig. 10(a) and (b). This small variation with respect to large misalignment has demonstrated that the resonance will maintain when using the integrated capacitor with some misalignment tolerance.

In practical applications, the self-inductance will vary slightly with the vertical and horizontal misalignment so does the mutual inductance [29-31]. As shown in Fig. 10(c), the mutual inductance with ferrite core drops faster than that without ferrite core after the horizontal misalignment of 100 mm. When the vertical misalignment is increased, the mutual inductances without ferrite core and with ferrite core decrease exponentially, as shown in Fig. 10(d).

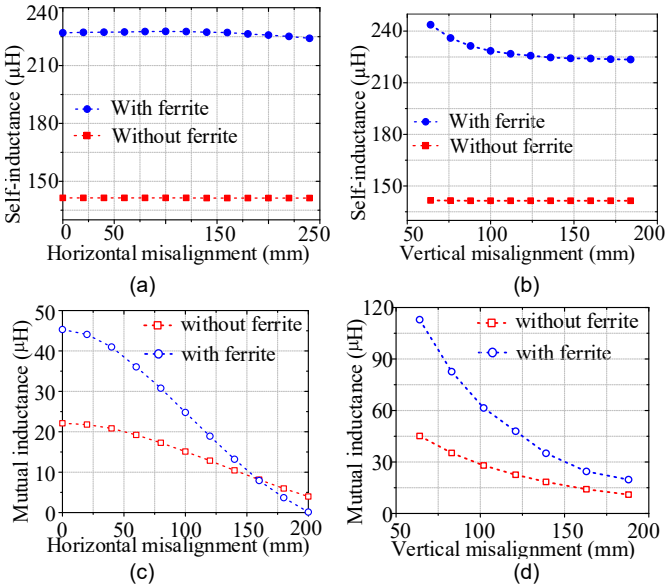

Fig. 10. Self-inductance and mutual inductance measurements when polypropylene coil pad as transmitter and polyimide coil pad as receiver are adopted. (a) Self-inductance with horizontal misalignments at the airgap of 120 mm. (b) Self-inductance with vertical misalignments. (c) Mutual inductance with horizontal misalignments at the airgap of 120 mm. (d) Mutual inductance with vertical misalignments.

B. Self-resonance of Capacitor-free Coil Pad

The capacitor-free coil can be regarded as an LC tank. By using the N4L IAI2 and PSM3750 as an LCR meter, the impedance and phase of the capacitorless coil at a range of frequency are measured. The impedance of the capacitor-free coil pads with and without ferrite cores are swept as shown in Fig. 11 and Fig. 12, respectively. The sweeping frequency is from 30 to 230 kHz with a resolution of every 0.1 kHz per sample. The resonance frequency is identified when the impedance is the minimum while the phase angle is zero.

It can be found that the self-resonant frequencies of mica, polypropylene, polyimide, and fiberglass capacitor-free coil pads are 122.5 kHz, 98.9 kHz, 92.5 kHz, and 100.3 kHz, respectively, without ferrite cores. Meanwhile, with the ferrite core, the self-resonant frequencies of mica, polypropylene, polyimide, and fiberglass capacitor-free coil pads are measured at 94.3 kHz, 76.9 kHz, 72.2 kHz, and 78.1 kHz, respectively. The desirable frequency range should be 80-90 kHz. However, due to the air bubbles in a multi-layer coil pad, the measured resonant frequencies are slightly shifted away.

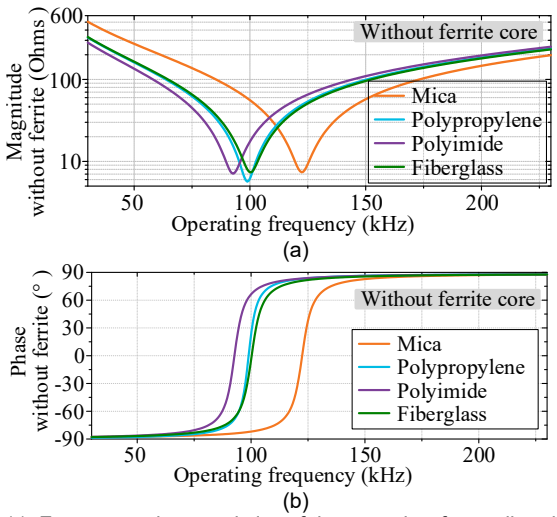

Fig. 11. Frequency characteristics of the capacitor-free coil pad without using ferrite core. (a) Impedances with four dielectrics. (b) Phase angle with four dielectrics.

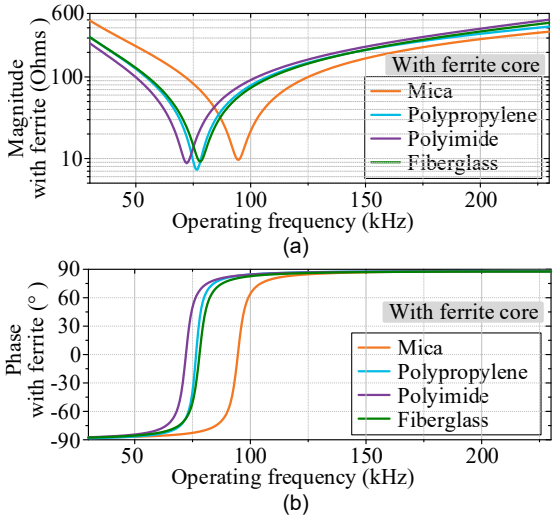

Fig. 12. Frequency characteristics of the capacitor-free coil pad with using ferrite core. (a) Impedances with four dielectrics. (b) Phase angle with four dielectrics.

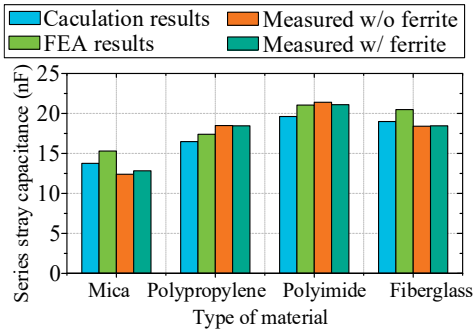

Fig. 13. Capacitance results among theoretical calculation, FEA simulation, and experimental measurement with different dielectric materials.

C. Series Integrated Compensation Capacitance

The capacitance results among theoretical calculation, FEA simulation, and experimental measurement are compared in Fig. 13. With ferrite cores, the compensation capacitances of

This article has been accepted for publication in a future issue of this journal, but has not been fully edited. Content may change prior to final publication. Citation information: DOI 10.1109/TIE.2020.3034867, IEEE Transactions on Industrial Electronics

mica coil pad, polypropylene coil pad, polyimide pad, and fiberglass coil pad are derived as 12.8 nF, 18.4 nF, 21.1 nF, and 18.5 nF, respectively. There is a small change for the capacitances between the pads with and without the ferrite cores. The errors between theoretical and measured results for mica, polypropylene, polyimide, and fiberglass coil pads are 8.3%, 11.4%, 6.0%, and 2.4%, respectively.

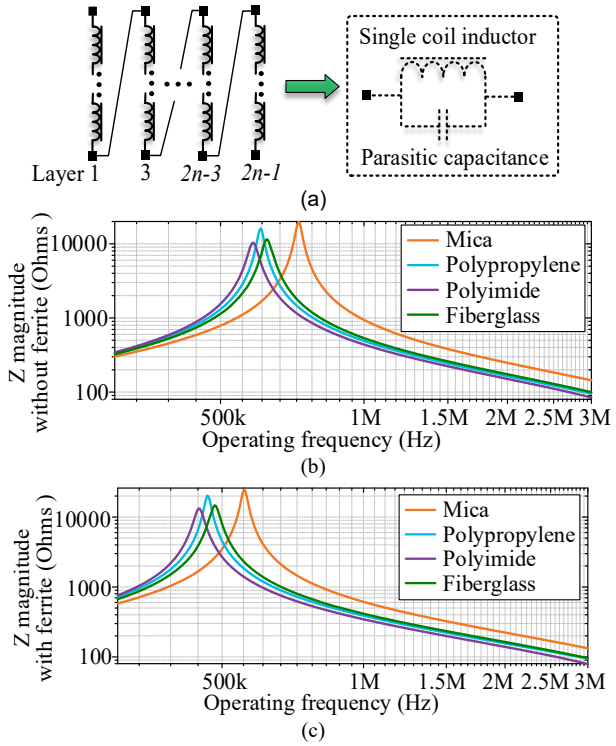

Fig. 14. Parasitic capacitance of a single coil inductor (directly connected group). (a) Equivalent circuit. (b) Impedance characteristics without ferrite core. (c) Impedance characteristics with ferrite core.

D. Parasitic Capacitance of Single Coil Inductor

Due to the high frequency operation and inserted multi-layer dielectrics, the undesirable parasitic capacitance of single coil inductor will be introduced and then lower the self-resonant frequency as shown in Fig. 14(a). In order to measure the parasitic capacitance, the impedance characteristics of single coil inductor without ferrite core are swept from 100 kHz to 3 MHz as shown in Fig. 14(b). The undesirable parasitic capacitance is calculated based on the measured impedance and the resonance. The measured resonance frequencies without ferrite core of mica coil pad, polypropylene coil pad, polyimide coil pad, and fiberglass coil pad are 730 kHz, 606 kHz, 585 kHz, and 625 kHz, respectively. The corresponding undesirable parasitic capacitances without ferrite core are achieved as 350 pF, 490 pF, 537 pF, and 475 pF.

After adding the ferrite core, as shown in Fig. 14(c), the undesirable parasitic capacitances are 367 pF, 503 pF, 556 pF, and 490 pF for mica coil pad, polypropylene coil pad, polyimide coil pad, and fiberglass coil pad. The ferrite core has a slight effect on the undesirable parasitic capacitance.

Deviation between the calculations and the measurement results has been observed which is caused by the assembling of coils. The impedance measurement uses an N4L IAI2 impedance analyser equipped with four internal shunts and a four-wire Kelvin connection. This impedance analyser is used in combination with the N4L PSM3750 phase sensitive multimeter to plot the impedance and phase with respect to frequency. The bandwidth of the impedance measurement of this set is from DC to 50 MHz. Since the resonance frequency of interest is around 85 kHz, the impact probe's resistance and capacitance for this measurement are negligible.

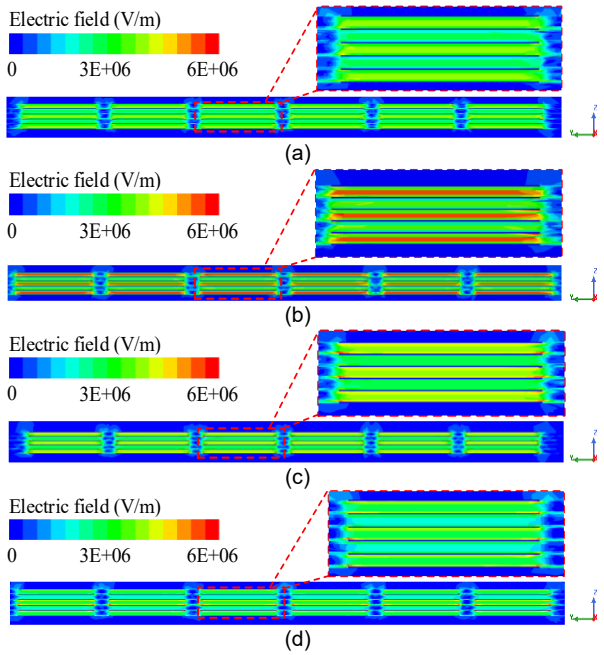

Fig. 15. Insulation evaluation based on electric field distributions. (a) Mica coil pad. (b) Polypropylene coil pad. (c) Polyimide coil pad. (d) Fiberglass coil pad.

E. Insulation Evaluation

Considering the multi-layer and multi-turn coil topology, the insulation should be analyzed to avoid possible breakdown between two adjacent turns and layers. The electric field distribution can be used to evaluate the insulation ability. When 20 A peak-to-peak current is injected into the capacitor-free coil pad at 85 kHz, the maximum potential difference can reach to 1.23 kV for each single inductor coil. The electric field distributions regarding different dielectrics are shown in Fig. 15. It can be seen that the electric field of the polypropylene coil pad is much higher than other coil pads due to its thinner thickness.

The FEA results show that all electric field distributions are significantly lower than the rated dielectric strengths listed in Tale I. Thus, it is verified that much higher current can be sustained and the selected dielectrics have a good insulation ability to suit the capacitor-free WPT system.

V. System Experimental Verification

An experimental setup has been built as shown in Fig. 16 in which the transmitter is a conventional capacitor compensated coil pad and the receiver is the proposed capacitor-free coil pad. The airgap between the transmitter and receiver is 120 mm, the inductance of the transmitter conventional coil is 205 μH, the load after rectifier is set at 61 Ω.

In order to match the self-resonant frequencies of the capacitor-free coil pads with mica, polypropylene, polyimide, and fiberglass, the capacitors with 14 nF, 20 nF, 22.2 nF, and

This article has been accepted for publication in a future issue of this journal, but has not been fully edited. Content may change prior to final publication. Citation information: DOI 10.1109/TIE.2020.3034867, IEEE Transactions on Industrial Electronics

20 nF are accordingly compensated for the conventional transmitter coil. The MAGNA-POWER TSD1000-20/415+HS DC supply is used. The high frequency AC input for the transmitter is generated by a SiC MOSFET (CREE, C3M0075120K) based H-bridge, which is operated with a duty ratio of 50%. The PWM signals were generated and controlled by the LAUNCHXL-F28379D. The deadtime is kept at 80 ns. The SiC diode rectifier employs SiC Schottky diodes (ON Semiconductor, 512-FFSH40120ADNF155). After that, the capacitance of 220 μF is used as a filter to reduce ripple voltage.

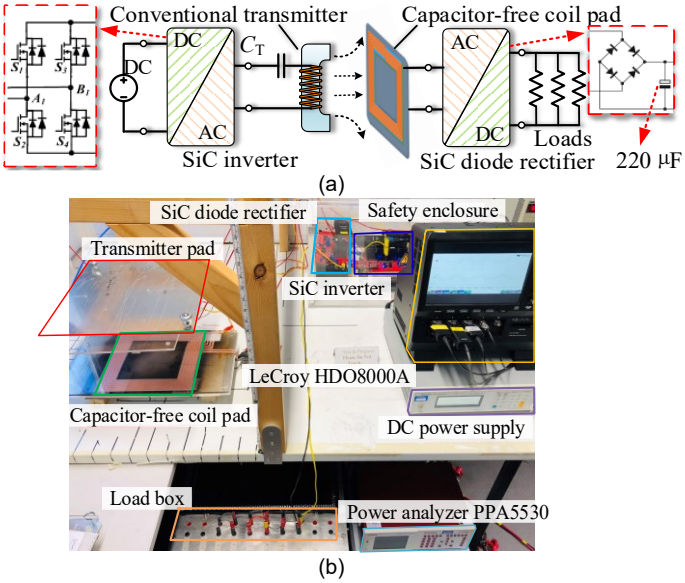

Fig. 16. Experimental setup of capacitor-free WPT system under lower operating frequency. (a) Setup schematic. (b) Setup prototype.

When the DC input voltage is 65 V and the operating frequency has been tuned to the self-resonant frequency of each capacitor-free coil pad, the measured voltage and current waveforms from LeCroy HDO8000A are shown in Fig. 17. It should be noticed that the gating setting needs to adapt the operating frequency to ensure accurate power measurement. Based on the measured waveforms, the received powers and transmission efficiencies are achieved for further comparison as listed in Table II. It can be found that the polypropylene coil pad presents the highest efficiency of 82% due to its thinner thickness thus lower dissipation factor tanδ of 0.014. It is worth noting that, the efficiency result is obtained from the system with only the receiver using capacitor-free self-resonant coil but the transmitter using the WPT conventional coil. The conventional WPT coil of the transmitter has an adjustable compensation circuit to facilitate different capacitor-free coils having different resonant frequencies.

The medium power WPT systems have potentials for mobile devices such as UAVs and electric scooters thus the receiver of the WPT is required to be small and light for such mobile devices. Although the capacitor-free coil can be applied at both the transmitter and the receiver, the advantage of lightweight and compactness of capacitor-free coils makes them more suitable for the receivers.

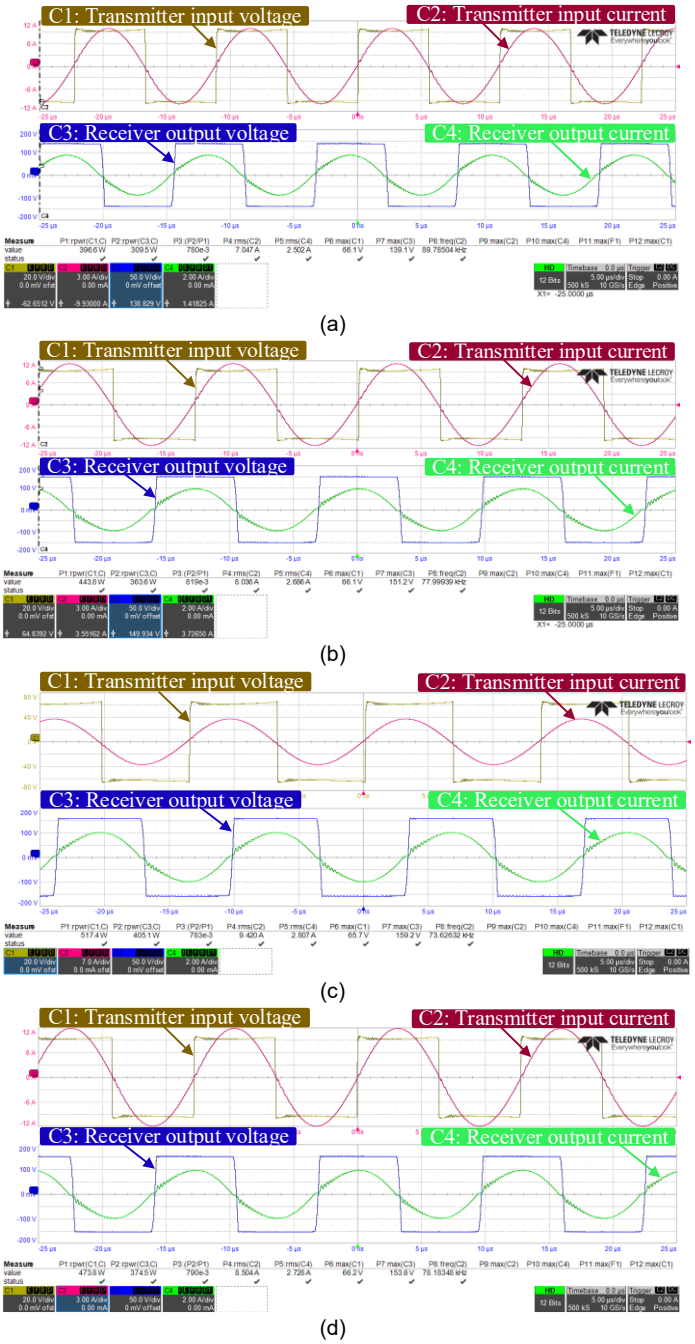

Fig. 17. Measured voltage waveforms, current waveforms, received power, and transmission efficiency with different dielectrics. (a) Mica coil pad. (b) Polypropylene coil pad. (c) Polyimide coil pad. (d) Fiberglass coil pad.

TABLE II. Experimental Comparison of Different Coils

Items	Mica	Polypropylene	Polyimide	Fiberglass
Received power (W)	309.5	363.6	405.1	374.5
Transmission efficiency	78%	82%	78.3%	79%
Dissipation factor tanδ	0.046	0.014	0.021	0.018

The received power distributions regarding different DC input voltage are shown in Fig. 18. It can be found that the tested power can reach up to 470 W and the highest transmission efficiency is 82% from the polypropylene coil pad. The loss breakdown of mica, polypropylene, polyimide, and fiberglass coil pads are shown in Fig. 18(a), (b), (c), and (d), respectively. In the power loss distributions, $P_{R\text{-}converter}$

This article has been accepted for publication in a future issue of this journal, but has not been fully edited. Content may change prior to final publication. Citation information: DOI 10.1109/TIE.2020.3034867, IEEE Transactions on Industrial Electronics

corresponds to the rectifier loss, $P_{T\text{-}cap}$ corresponds to compensation capacitor loss at the transmitter side, $P_{T\text{-}coil}$ corresponds to the copper loss of the transmitter coil, $P_{R\text{-}cap}$ corresponds to the capacitance loss of the proposed capacitor-free coil pad, $P_{R\text{-}coil}$ corresponds to the copper loss of the proposed capacitor-free coil pad. All power loss distributions are under the input voltage of 65 V and the received power of the capacitor-free coils with mica, polypropylene, polyimide, and fiberglass are 312.1 W, 367.7 W, 405.3 W, and 370.8 W, respectively. Meanwhile, the corresponding efficiencies of the mica, polypropylene, polyimide, and fiberglass coils are 77.2%, 81.8%, 78.3%, and 78.7%, respectively.

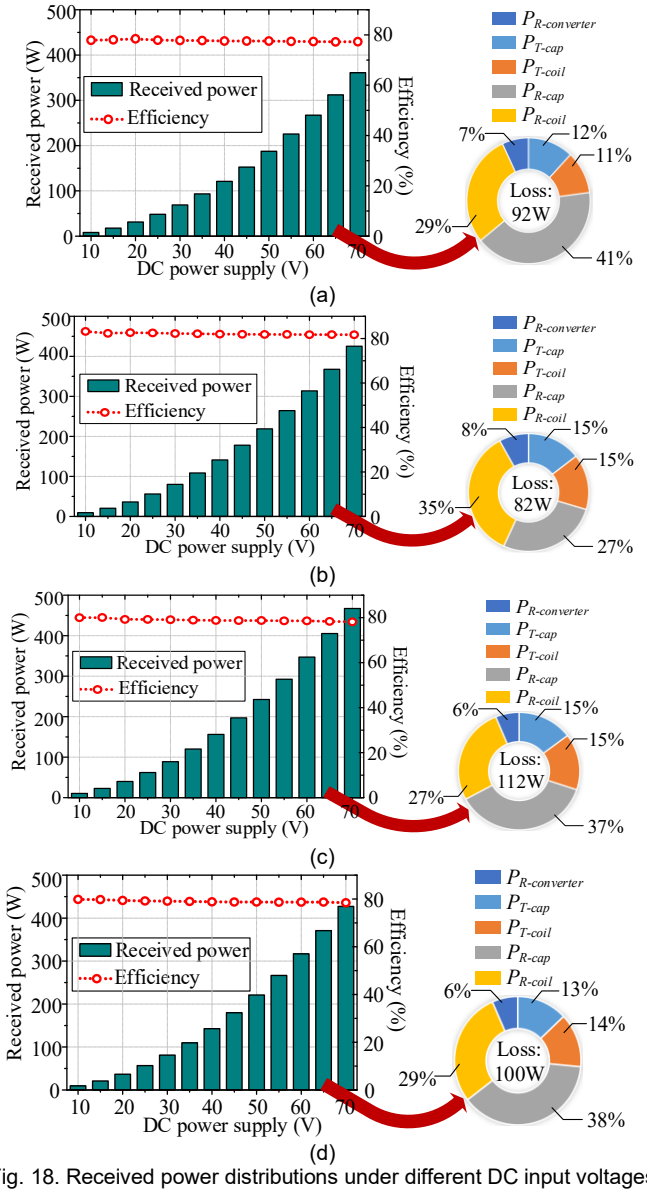

Fig. 18. Received power distributions under different DC input voltages and power losses distribution. (a) Mica coil pad. (b) Polypropylene coil pad. (c) Polyimide coil pad. (d) Fiberglass coil pad.

Due to the skin effect at the high operating frequency near the self-resonance frequency, the AC resistance will account for the most of the total resistance [32-34]. The skin depth is 0.22 mm for copper at 85 kHz thus the maximum effective thickness for conduction of each turn is 0.44 mm. This effective thickness for conduction at 85 kHz is considerably larger than that operating at hundreds kHz or MHz in other capacitor-free IPT wireless power transfer systems, thus more room for increasing the foil thickness to reduce the copper loss at lower resonance frequencies such as 85 kHz. The foil used for the coil in this paper has a thickness of 0.04 mm which can be increased by severalfold in order to reduce the copper loss and then improve the transmission efficiency. It should be noticed that the receiver capacitor loss of polypropylene coil pad is the smallest of that among all four coils.

A comparison between the multi-layer capacitor-free coil and the conventional wireless charging coil having the same power rating has been given in Table III.

TABLE III. Comparison of the proposed capacitor-free coil and conventional WPT coil with the same power design of 400 W.

Items	Multi-layer capacitor-free coil	Conventional WPT coil with compensation circuit [1]
Prototype	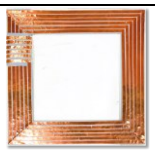	
Operating frequency	**80-120 kHz**	**81.38-90.0 kHz**
Quality factor	**23**	**56**
Efficiency	**82%**	**91%**
Weight	**97.1 g** (Due to printable copper foil, and no compensation capacitors)	**187.1 g** (Due to Litz wires, and compensation capacitors)
Power density[2]	Gravimetric: 10.29 W/cm^3 Volumetric: 4.12 W/g	Gravimetric: 7.26 W/cm^3 Volumetric:2.44 W/g
Additional capacitor	**N/A**	**15 nF** EPCOS PP capacitor 1kV DC voltage
Coil thickness	**0.96 mm**	**1.44 mm**

1 All comparisons are based on the same power rating (400 W) design for the proposed capacitor-free WPT system and the conventional WPT system.
2 The power density is calculated for the resonant circuit excluding the converters.

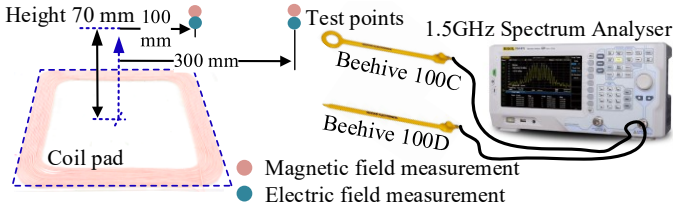

Fig. 19. The prototype to measure the electric field and the magnetic field at different positions.

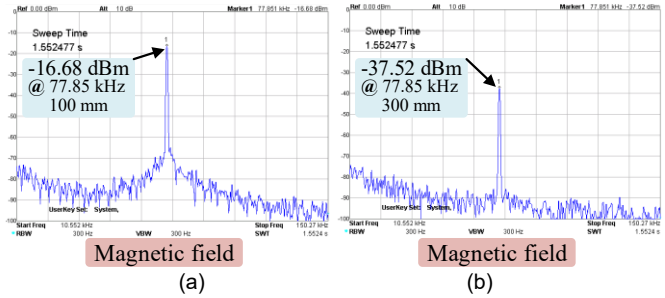

This article has been accepted for publication in a future issue of this journal, but has not been fully edited. Content may change prior to final publication. Citation information: DOI 10.1109/TIE.2020.3034867, IEEE Transactions on Industrial Electronics

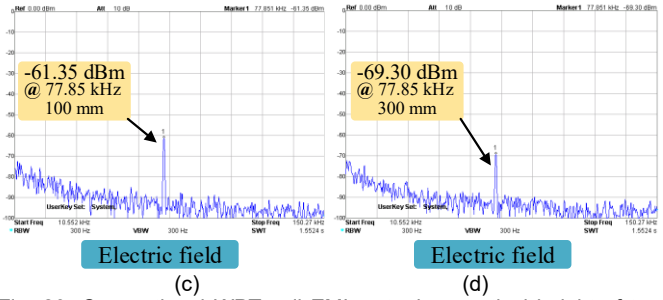

Fig. 20. Conventional WPT coil EMI test when vertical height of test point is set at 70 mm. (a-b) Magnetic field at horizontal distance of 100 mm, and 300 mm. (c-d) Electric field at horizontal distance of 100 mm, and 300 mm.

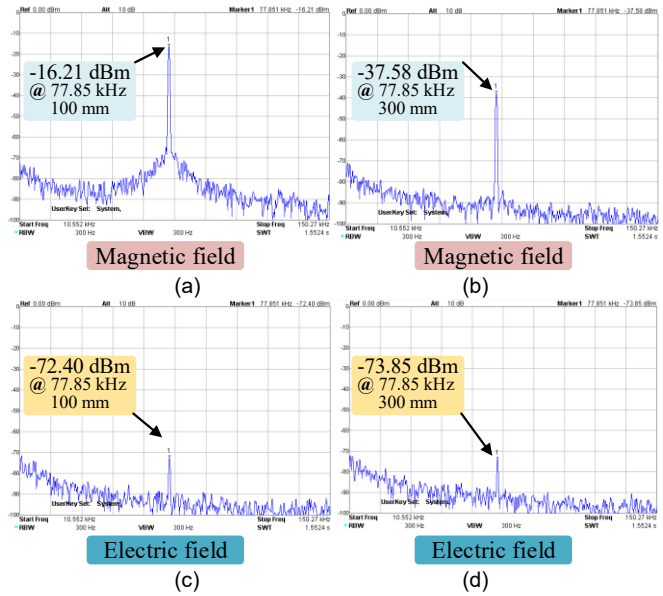

Fig. 21. Proposed capacitor-free coil EMI test when vertical height of test point is set at 70 mm. (a-b) Magnetic field at horizontal distance of 100 mm, and 300 mm. (c-d) Electric field at horizontal distance of 100 mm, and 300 mm.

Considering the EMI issue, the electric field and the magnetic field at different positions are measured as shown in Fig. 19, where the compared conventional WPT coil is designed with the same power of 400 W. The Beehive 100C is applied to measure the magnetic field and the Beehive 100D is applied to measure the electric field. The RIGOL DSA815 is used as a spectrum analyser. The EMI measured results of the conventional WPT coil and the capacitor-free coil are shown in Fig. 20 and Fig. 21, respectively. In terms of the magnetic field, there is no obvious difference between the conventional WPT coil and the capacitor-free coil under the same current with peak value of 4 A. In terms of the electric field, that of the capacitor-free coil is slightly lower than that of the conventional WPT coil. It is because that the multi-layer copper foils also behave as a shield. As a result, the proposed capacitor-free coil would not introduce serious EMI problems when comparing to the conventional WPT system.

With the aim to further evaluate the frequency response, the received powers with frequency sweeping have been conducted to compare the difference between the capacitor-free coil and the conventional WPT coil, as shown in Fig. 22. It can be found that when the input power is kept the same with varying frequencies, the frequency responses of the capacitor-free coil and the conventional WPT coil are the same.

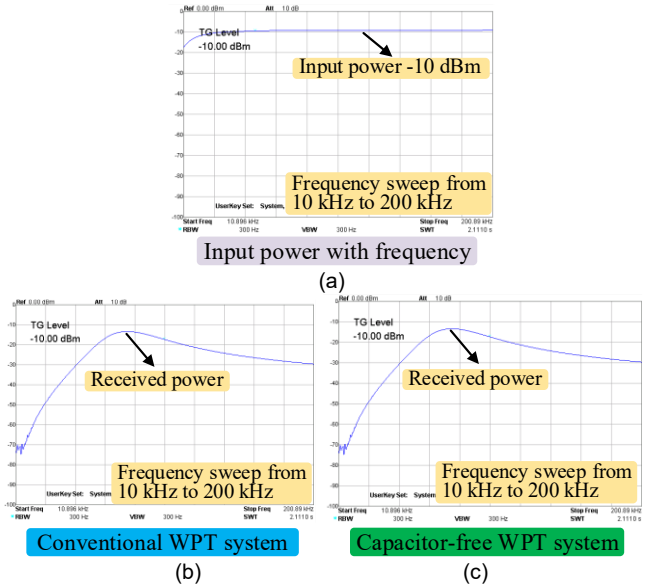

Fig. 22. Frequency response analysis for the proposed capacitor-free coil and the conventional WPT coil. (a) Fixed input power of -10 dBm with frequency variation. (b) Received power of the conventional WPT system. (c) Received power of the capacitor-free system.

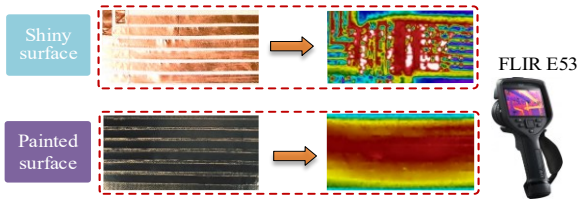

Fig. 23. Emissivity enhancement for the copper foil by painting the surface with black acrylic paint.

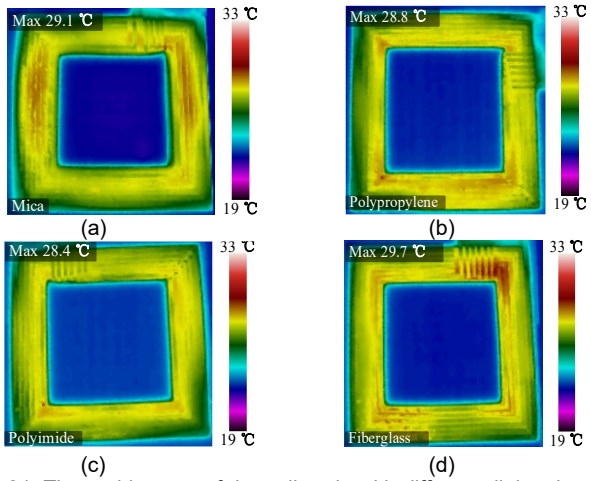

Fig. 24. Thermal images of the coil pads with different dielectrics after the black acrylic painting. (a) Mica coil pad. (b) Polypropylene coil pad. (c) Polyimide coil pad. (d) Fiberglass coil pad.

The thermal performance is captured by a thermal imaging camera FLIR E53. The emissivity is enhanced by painting the black acrylic paint on the copper foil for the thermally reflective surface as shown in Fig. 23. The thermal images of the proposed coil pads are presented as shown in Fig. 24. The ambient temperature is 20 ℃ with a current of 5 A peak-to-

peak value. The maximum temperatures of all coil pads are under 33°C.

All experimental results verify the feasibility of the proposed capacitor-free coil pads for the medium power WPT system. The polypropylene possesses the lowest loss. The performance should be further improved by using better fabrication and reducing the adhesion layers. In order to increase the power rating and reduce the copper loss, thicker copper foil or more copper layers can be added at the same layer winding.

VI. Conclusion

In this paper, multi-layer capacitor-free self-resonant WPT coil pads with four dielectrics are proposed and implemented. The proposed system has been experimentally verified at 470 W received power by using copper foil with only 0.04 mm thickness. The multi-layer topology integrates the inductance and capacitance into one single coil pad, the compensation capacitor for the WPT system can be eliminated. The self-resonant circuit with multi-layer topology has been modeled and simplified. The fringing effect has been analyzed to evaluate the undesirable parasitic capacitance in a single coil inductor. The insulation between the two coil layers has been evaluated. Both the simulation and experimental results have been provided to verify the proposed capacitor-free WPT system. The thermal images have shown that the proposed capacitor-free coil pads are also thermally feasible.

Appendix

When considering the single-layer fringing effect, the parasitic capacitance between turn and turn can be calculated based on the conformal mapping and the assumption of the magnetic wall. All symbols listed in the following equations have been indicated in Fig. 6.

Thus, the capacitance with the air is calculated by

$$\begin{cases} k_0 = \dfrac{d_{air}}{w_{turn}} \\ C_{air} = l_{foil}\varepsilon_0 F(k_0) \end{cases} \tag{20}$$

The capacitance with the foil adhesion is calculated by

$$\begin{cases} k_1 = \tanh(\dfrac{\pi d_{air}}{4d_1}) / \tanh(\dfrac{\pi w_{turn}}{4d_1}) \\ C_{coilad} = \dfrac{1}{2} l_{foil}\varepsilon_0(\kappa_2 - \kappa_1)F(k_1) \end{cases} \tag{21}$$

The capacitance with the dielectric is calculated by

$$\begin{cases} k_2 = \tanh(\dfrac{\pi d_{air}}{4(d_1+d_2)}) / \tanh(\dfrac{\pi w_{turn}}{4(d_1+d_2)}) \\ C_{die} = \dfrac{1}{2} l_{foil}\varepsilon_0(\kappa_2 - \kappa_3)F(k_2) \end{cases} \tag{22}$$

The capacitance with the dielectric adhesion is calculated by

$$\begin{cases} k_3 = \tanh(\dfrac{\pi d_{air}}{4(d_1+d_2+d_3)}) / \tanh(\dfrac{\pi w_{turn}}{4(d_1+d_2+d_3)}) \\ C_{diead} = \dfrac{1}{2} l_{foil}\varepsilon_0(\kappa_3 - 1)F(k_3) \end{cases} \tag{23}$$

where the $F(k_i)$ (i=0, 1, 2, 3, 4) is expressed as

$$F(k_i) = \begin{cases} \pi^{-1} \ln\left[2\dfrac{1+(1-k_i^{\,2})^{0.25}}{1-(1-k_i^{\,2})^{0.25}} \right] & \text{for } k_i^{\,2} \le 0.5 \\ \pi\left[\ln\left(2\dfrac{1+k_i^{\,0.5}}{1-k_i^{\,0.5}} \right) \right]^{-1} & \text{for } k_i^{\,2} \ge 0.5 \end{cases} \tag{24}$$

References

[1] N. Tesla, "The transmission of electrical energy without wires," *Electrical World and Engineer*, Mar., 1904.

[2] M. Budhia, J. T. Boys, G. A. Covic, and C. Y. Huang, "Development of a single-sided flux magnetic coupler for electric vehicle ipt charging systems," *IEEE Transactions on Industrial Electronics,* vol. 60, no. 1, pp. 318-328, Dec., 2013.

[3] S. Y. R. Hui, W. Zhong, and C. K. Lee, "A critical review of recent progress in mid-range wireless power transfer," *IEEE Transactions on Power Electronics,* vol. 29, no. 9, pp. 4500-4511, Sept., 2014.

[4] C. C. Mi, G. Buja, S. Y. Choi, and C. T. Rim, "Modern advances in wireless power transfer systems for roadway powered electric vehicles," *IEEE Transactions on Industrial Electronics,* vol. 63, no. 10, pp. 6533-6545, Oct., 2016.

[5] C. Jiang, K. T. Chau, C. Liu, and W. Han, "Design and analysis of wireless switched reluctance motor drives," *IEEE Transactions on Industrial Electronics,* vol. 66, no. 1, pp. 245-254, Jan., 2019.

[6] H. Zeng, S. Yang, and F. Z. Peng, "Design consideration and comparison of wireless power transfer via harmonic current for phev and ev wireless charging," *IEEE Transactions on Power Electronics,* vol. 32, no. 8, pp. 5943-5952, 2016.

[7] Z. Zhang, K. T. Chau, C. Qiu, and C. Liu, "Energy encryption for wireless power transfer," *IEEE Transactions on Power Electronics,* vol. 30, no. 9, pp. 5237-5246, Sept., 2015.

[8] J. Zhou, B. Zhang, W. Xiao, D. Qiu, and Y. Chen, "Nonlinear parity-time-symmetric model for constant efficiency wireless power transfer: Application to a drone-in-flight wireless charging platform," *IEEE Transactions on Industrial Electronics,* vol. 66, no. 5, pp. 4097-4107, Jan., 2018.

[9] S. Obayashi, Y. Kanekiyo, K. Nishizawa, and H. Kusada, "85-kHz band 450-W inductive power transfer for unmanned aerial vehicle wireless charging port." in *2019 IEEE Wireless Power Transfer Conference (WPTC)*, pp. 80-84, June, 2019.

[10] S. J. Huang, T. S. Lee, W. H. Li, and R. Y. Chen, "Modular on-road AGV wireless charging systems via interoperable power adjustment," *IEEE Transactions on Industrial Electronics,* vol. 66, no. 8, pp. 5918-5928, Aug., 2018.

[11] C. M. D Miranda, and S. F. Pichorim, "A self-resonant two-coil wireless power transfer system using open bifilar coils," *IEEE Transactions on Circuits and Systems II: Express Briefs,* vol. 64, no. 6, pp. 615-619, June, 2016.

[12] R. Narayanamoorthi, and A. V. Juliet, "Capacitor-less high-strength resonant wireless power transfer using open bifilar spiral coil," *IEEE Transactions on Applied Superconductivity,* vol. 29, no. 1, pp. 1-8, Jan., 2018.

[13] K. Furusato, T. Imura, and Y. Hori, "Design of multi-frequency coil for capacitor-less wireless power transfer using high order self-resonance of open end coil." in *2016 IEEE Wireless Power Transfer Conference (WPTC)*, pp. 1-4, June, 2019.

[14] J. Kuipers, H. Bruning, D. Yntema, S. Bakker, and H. Rijnaarts, "Self-capacitance and resistive losses of saline-water-filled inductors," *IEEE Transactions on Industrial Electronics,* vol. 61, no. 5, pp. 2356-2361, May, 2013.

[15] K. Chen, and Z. Zhao, "Analysis of the double-layer printed spiral coil for wireless power transfer," *IEEE Journal of Emerging and Selected Topics in Power Electronics,* vol. 1, no. 2, pp. 114-121, July, 2013.

[16] Q. Li, and Y. C. Liang, "An inductive power transfer system with a high-Q resonant tank for mobile device charging," *IEEE Transactions on power electronics,* vol. 30, no. 11, pp. 6203-6212, Nov., 2015.

[17] A. L. Stein, P. A. Kyaw, and C. R. Sullivan, "Wireless power transfer utilizing a high-Q self-resonant structure," *IEEE Transactions on Power Electronics,* vol. 34, no. 7, pp. 6722-6735, July, 2018.

[18] Y. Alazzawi, K. Aono, E. L. Scheller, and S. Chakrabartty, "Exploiting self-capacitances for wireless power transfer," *IEEE transactions on biomedical circuits and systems,* vol. 13, no. 2, pp. 425-434, April, 2019.

[19] B. Breitkreutz, and H. Henke, "Calculation of self-resonant spiral coils for wireless power transfer systems with a transmission line approach," *IEEE Transactions on Magnetics,* vol. 49, no. 9, pp. 5035-5042, Sept., 2013.
[20] R. S. Y. Hui, "Planar wireless charging technology for portable electronic products and Qi," *Proceedings of the IEEE,* vol. 101, no. 6, pp. 1290-1301, Mar., 2013.
[21] C. Xia, L. Liu, Y. Liu, and Z. Ma, "Ipt system for tail-free household appliances in the smart home system," *IET Power Electronics,* vol. 12, no. 5, pp. 1002-1010, Jan., 2019.
[22] K. Y. G. Ho, and B. M. Pong, "Multilayer flexible printed circuitry planar transformer with integrated series capacitance for LLC converter," *IEEE Transactions on Power Electronics,* vol. 34, no. 11, pp. 11139 - 11152, Feb., 2019.
[23] L. Dalessandro, F. D. S. Cavalcante, and J. W. Kolar, "Self-capacitance of high-voltage transformers," *IEEE Transactions on Power Electronics,* vol. 22, no. 5, pp. 2081-2092, Sept., 2007.
[24] T. Grove, M. Masters, and R. Miers, "Determining dielectric constants using a parallel plate capacitor," *American journal of physics,* vol. 73, no. 1, pp. 52-56, Dec., 2005.
[25] A. K. Verma, P. Singh, and L. Matekovits, "Strip-width and slot-gap dependent equivalent isotropic substrate and dispersion characteristics of asymmetric coplanar waveguide, symmetric coplanar waveguide and micro-coplanar strip line on anisotropic substrates," *IEEE Transactions on Microwave Theory and Techniques,* vol. 62, no. 10, pp. 2232-2241, Oct., 2014.
[26] O. Vendik, S. Zubko, and M. Nikol'Skii, "Modeling and calculation of the capacitance of a planar capacitor containing a ferroelectric thin film," *Technical Physics,* vol. 44, no. 4, pp. 349-355, April, 1999.
[27] Z. Shen, H. Wang, Y. Shen, Z. Qin, and F. Blaabjerg, "An improved stray capacitance model for inductors," *IEEE Transactions on Power Electronics,* vol. 34, no. 11, pp. 11153-11170, Mar., 2019.
[28] F. Jolani, Y. Yu, and Z. Chen, "A planar magnetically coupled resonant wireless power transfer system using printed spiral coils," *IEEE Antennas and Wireless Propagation Letters,* vol. 13, pp. 1648-1651, Aug., 2014.
[29] P. Si, A. P. Hu, S. Malpas, and D. Budgett, "A frequency control method for regulating wireless power to implantable devices," *IEEE transactions on biomedical circuits and systems,* vol. 2, no. 1, pp. 22-29, Mar., 2008.
[30] Z. Huang, S. C. Wong, and K. T. Chi, "Control design for optimizing efficiency in inductive power transfer systems," *IEEE Transactions on Power Electronics,* vol. 33, no. 5, pp. 4523-4534, May, 2017.
[31] Y. Jiang, L. Wang, Y. Wang, M. Wu, Z. Zeng, Y. Liu, and J. Sun, "Phase-locked loop combined with chained trigger mode used for impedance matching in wireless high power transfer," *IEEE Transactions on Power Electronics,* vol. 35, no. 4, pp. 4272-4285, April, 2019.
[32] Y. Tokudaiji, D. Miura, Y. Hattori, K. Murasato, Y. Bu, and T. Mizuno, "AC resistance reduction of a flexible wireless power transmission coil using magnetic path control technology at 13.56 MHz," *IEEE Transactions on Magnetics,* vol. 55, no. 7, pp. 1-7, Mar., 2019.
[33] J. Kim, and Y. J. Park, "Approximate closed-form formula for calculating ohmic resistance in coils of parallel round wires with unequal pitches," *IEEE transactions on Industrial Electronics,* vol. 62, no. 6, pp. 3482-3489, June, 2014.
[34] G. Zhu, and R. D. Lorenz, "Surface spiral parallel and antiparallel winding designs for high efficiency, low spatial voltage stress, and inductive wireless power transfer systems," *IEEE Transactions on Industry Applications,* vol. 55, no. 1, pp. 741-750, Jan., 2018.

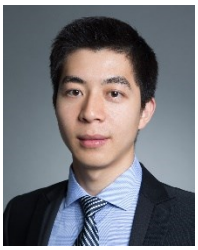

Chaoqiang Jiang (S'16–M'19) received the B.Eng. and M.Sc. degrees in electrical engineering and automation from Wuhan University, Wuhan, China, in 2012 and 2015, respectively, and the Ph.D. degree in electrical and electronic engineering from The University of Hong Kong, Hong Kong, in 2019.

He is currently a Postdoctoral Research Associate at the University of Cambridge, U.K. In 2019, he was a Visiting Researcher at the Nanyang Technological University, Singapore. His current research interests include power electronics, wireless power transfer techniques, electric machines and drives, and electric vehicle (EV) technologies.

Daniel E. Gaona (S'14) received the B.S. degree in electrical engineering and the B.S. degree in mechanical engineering from the San Francisco de Quito University, Quito, Ecuador, in 2013 and 2014, respectively. In 2016, he received the M.Sc. degree in electrical engineering from the Erasmus Mundus Master Course (EMMC) Consortium.

In 2017, he worked at the Department of Power Electronics and Electrical Drives at the University of Paderborn, Germany, as a Research Associate. In 2018, he joined the University of Cambridge and he is currently working towards his Ph.D. degree. His research interests include electric drives, power electronics, and wireless charging systems.

Yanfeng Shen (S'16–M'18) received the B.Eng. degree in electrical engineering and automation and the M.Sc. degree in power electronics from Yanshan University, Qinhuangdao, China, in 2012 and 2015, respectively, and the Ph.D. degree in power electronics from Aalborg University, Aalborg, Denmark, in 2018.

He is currently a Postdoctoral Research Associate at the University of Cambridge, UK. He worked as an Intern with ABB Corporate Research Center, Beijing, China, in 2015. He was a Visiting Graduate Research Assistant with Khalifa University, UAE, in 2016. His current research interests include the thermal management and reliability of power electronics, electric vehicle (EV) traction inverters, and applications of SiC and GaN power devices.

Hui Zhao (S'14–M'18) received the bachelor and master degrees in electrical engineering from Huazhong University of Science and Technology, Wuhan, China, in 2010 and 2013, respectively, and the Ph.D. degree in power electronics from the Universality of Florida, Gainesville, FL, USA, in 2018.

He had a Summer Internship with General Electric Global Research Center, Shanghai, in 2013. He is currently a Postdoctoral Research Associate with the University of Cambridge, Cambridge, UK. His research interests include the modeling and driving of the power devices, EMI, and the high power density power converters.

K. T. Chau (M'89–SM'04–F'13) received the B.Sc.(Eng.), M.Phil., and Ph.D. degrees in electrical and electronic engineering from The University of Hong Kong, Pokfulam, Hong Kong, in 1988, 1991, and 1993, respectively.

Since 1995, he has been with The University of Hong Kong, where he currently serves as Professor and Head of Department in the Department of Electrical and Electronic Engineering. He is the author of seven books and more than 300 journal papers. His research interests include electric and hybrid vehicles, power electronics and drives, and renewable energies.

Prof. Chau was the recipient of the Changjiang Chair Professorship from the Ministry of Education, China, and the Environmental Excellence in Transportation Award for Education, Training, and Public Awareness from the Society of Automotive Engineers International. He is a Fellow of the Institution of Engineering and Technology (IET), U.K., and also, of the Hong Kong Institution of Engineers. He is currently also a Co-editor of the Journal of Asian Electric Vehicles. He is a Chartered Engineer in Hong Kong.

Teng Long (M'13) received the B.Eng. degree from the Huazhong University of Science and Technology, China, the first class B.Eng. (Hons.) degree from the University of Birmingham, UK in 2009, and the Ph.D. degree from the University of Cambridge, UK in 2013.

Until 2016, he was a Power Electronics Engineer with the General Electric (GE) Power Conversion business in Rugby, UK. He is currently a Lecturer with the University of Cambridge. His research interests include power electronics, electrical machines, and machine drives. Dr Long is a Chartered Engineer (CEng) registered with the Engineering Council in the UK.